Structural and vibrational behavior of cubic $Cu_{1.80(3)}Se$ cuprous selenide, Berzelianite, under compression

R. Chuliá-Jordan[1], D. Santamaría-Pérez[1,*], A.L.J. Pereira[2,3], B. García-Domene[1], R. Vilaplana[2], J.A. Sans[2], D. Martínez-García[1], A. Morales-Garcia[4], C. Popescu[5], C. Muehle[6], M. Jansen[6], F.J. Manjón[2]

[1] Departamento de Física Aplicada-ICMUV, MALTA-Consolider Team, Universitat de Valencia, E-46100 Burjassot, Valencia, Spain
[2] Instituto de Diseño para la Fabricación y Producción Automatizada, MALTA-Consolider Team, Universitat Politècnica de València, E-46022 Valencia, Spain
[3] Grupo de Pesquisa de Materiais Fotonicos e Energia Renovável - MaFER, Universidade Federal da Grande Dourados, Dourados, MS, Brazil
[4] Departamento de Ciencia de Materiales y Química-Física, Universidad de Barcelona, E-08028, Barcelona, Spain
[5] CELLS-ALBA Synchrotron Light Facility, Cerdanyola del Vallès, 08290, Barcelona, Spain
[6] Max-Planck Institut fuïr Festkoïrperforschung, Heisenbergstrasse 1, 70569 Stuttgart, Germany

Abstract

We have performed an experimental study of the crystal structure and lattice dynamics of cubic $Cu_{1.80(3)}Se$ at ambient temperature and high pressures. Two reversible phase transitions were found at 2.9 and 8.7 GPa. The indexation of the angle-dispersive synchrotron x-ray diffraction patterns suggests a large orthorhombic cell and a monoclinic cell for the high-pressure phases. Raman measurements provide additional information on the local structure. The compressibility of the three ambient temperature phases has been determined and compared to that of other sulphides and selenides.

Introduction

$Cu_{2-x}Se$ cuprous selenides have attracted great interest from the physical and technological point of view because they are cheap high performing thermoelectric materials [1-3]. Stoichiometric Cu_2Se, for instance, acquires superionic conductivity above 400 K and a zT thermoelectric figure of merit of 1.5 at 1000 K [1,2]. Colossal values of the Seebeck coefficient in the temperature range of 340−400 K have been also recently reported, possessing unusually high values of power factor exceeding 2.3 $Wm^{-1}K^{-2}$ in both parallel and perpendicular directions of electrical current [3]. In addition to these interesting properties, it is known that non-stoichiometric $Cu_{2-x}Se$ is an excellent p-type electrical conductor, which increases its conductivity with Cu deficiency as a result of the

formation of equivalent concentration of holes. Therefore, the composition of copper selenide alters its electronic, chemical and thermal properties, being a versatile compound for a vast range of applications, from counter electrodes in solar cells to flexible electronic and thermoelectric materials [4]. Intensive research on these materials is active nowadays, looking for further unusual behaviors in transport properties.

In order to fully understand the physical properties of copper selenides, the crystal structures of Cu_2Se and slightly stoichiometry-deviated $Cu_{2-x}Se$ ($0<x<0.2$) have been studied for a long time [5-15]. In spite of their simple chemical formula, these compounds have quite complex atomic arrangements. The phase diagram of the $Cu_{2-x}Se$ region exhibits two phases, a low-temperature α-phase and a high-temperature β-phase [5,6]. The structure of the room temperature α-Cu_2Se phase is known to be a distortion of the antifluorite-type (aF) cubic structure stable at high temperatures, but remains still controversial. Thus, initially, Borchert reported a tetragonal cell [7]. Subsequently, different authors proposed an orthorhombic [10] and three monoclinic unit-cells [11-13] from x-ray powder diffraction and electron microscopy studies. Later, the structure of α-Cu_2Se was solved by single-crystal x-ray diffraction, after obtaining a twinning-free specimen. It was described using a C2/c monoclinic space group with lattice parameters a=7.1379(4), b=12.3823(7) and c=27.3904(9) Å, and a β angle of 94.31º [14]. More recently, Eikeland and coworkers reported another solution for the room-temperature Cu_2Se structure: a rhombohedral phase related to the aF structure through symmetry reduction, with lattice parameters a= 4.1227(8) and c = 20.449(6) Å [15]. The crystal structure of copper selenides is therefore rather complex and the existence of a very narrow compositional-dependent crystal stability range, as occurs in Cu_2S [16], that could give rise to different room-temperature phases, cannot be ruled out.

The low-symmetry α-Cu_2Se phase is stable up to about 400 K [5,6], where it fully transforms into the cubic $Fm\bar{3}m$ aF-type phase (named β). This high-temperature polymorph has the Se atoms in a simple fcc arrangement and the Cu ions are kinetically disordered throughout the structure, unlike the α-phase where they are localized. The presence of a crystalline sublattice surrounded by liquid-like Cu ions made copper chalcogenides promising high-efficiency thermoelectric materials. Note that increasing Cu deficiency in $Cu_{2-x}Se$ makes the cubic aF structure stabilize at lower temperatures, which led $Cu_{1.80}Se$ to be stable at ambient temperature [5]. Thus, this cubic polymorph of copper selenide is found in nature in mineral form, named Berzelianite, with approx. chemical formula $Cu_{1.85}Se$ after specific gravity measurements on several specimens [8] (see the crystal structure depicted in Figure 1).

Pressure, like temperature and composition, is a thermodynamic parameter that can strongly modify the atomic interaction in covalent solids. High pressure studies in materials science have led to: (i) the synthesis of novel materials [17] and chemical reactivity routes [18,19], (ii) phase transformations [20-22], and (iii) the uncovering of structural underlying systematics [23,24]. Whereas the structural evolution of copper-rich selenides with temperature was thoroughly studied, only three studies devoted to the structural high pressure modifications exist in literature [9,11,25]. Hinze & Neuhaus carried out an x-ray diffraction investigation on Cu_2Se up to 8 GPa, but the fact that their initial structure was cubic aF berzelianite points to a Cu–defective starting phase. They reported that it disproportionates firstly into Cu_3Se_2 Umangite + Cu at 2.2 GPa, then into $CuSe_2$ marcasite-type + Cu at 3.7 GPa and, finally, that marcasite-type structure transforms into a pyrite-type one at 4.4 GPa [9]. The authors also claimed that Cu metal diffused to perimeter areas of the

sample and precipitated in the form of spherical aggregates. This behavior contrasts with the pressure effect reported on other binary chalcogenides, where no dissociation was observed [26-34]. Later, Murray and Heyding studied several copper selenides up to 5 GPa and found the $\alpha \rightarrow \beta$ transition in monoclinic Cu_2Se at different P – T conditions, but no disproportionation in cubic $Cu_{2-x}Se$ up to the maximum pressure [11]. A more recent x-ray diffraction study reported two pressure-induced structural transitions on monoclinic Cu_2Se at 3.3 and 7.4 GPa without signs of decomposition, and identified the high-pressure phases using the CALYPSO methodology for structure prediction (which combines first-principle calculations with global minimization of the free energy) [25].

The present study investigates the high-pressure behavior of Cu-defective $Cu_{1.80(3)}Se$, which adopts the cubic anti-fluorite structure at ambient conditions. We performed angle-dispersive synchrotron-radiation powder X-ray diffraction and Raman spectroscopy measurements up to 20 GPa under quasi-hydrostatic conditions. Our results differ from those of Hinze and Neuhaus [9], and from those of Murray and Heyding [11], performed under non-hydrostatic conditions, and evidence the complex crystal chemistry of copper-rich chalcogenides.

Experimental details

The polycrystalline $Cu_{1.80(3)}Se$ sample was synthesized from the elements by heating twice at 400ºC and 250ºC in evacuated quartz ampoules over 3 days. Elemental analyses carried out in a Philips XL30 scanning electron microscope using energy dispersive x-ray spectroscopy confirmed its stoichiometry. Powder X-ray diffraction (XRD) with Cu Kα radiation of the black metallic product evidenced the formation of the cubic aF berzelianite structure.

High-pressure angle-dispersive XRD measurements were carried out in the Materials Science and Powder Diffraction (MSPD) station of the ALBA-CELLS synchrotron light source using a monochromatic wavelength of 0.4246 Å and a beam focused to 30 μm^2. Diffraction patterns were collected on a MAR345 charge-coupled device (CCD) detector. A precise calibration of the detector parameters was developed with a reference LaB_6 powder for distortion, and integration to conventional 2θ-intensity data was carried out with the Fit2D software [35]. For high-pressure measurements, the $Cu_{1.80(3)}Se$ sample was placed in the stainless-steel gasket cavity inside a membrane diamond-anvil cell (mDAC), along with two ruby chips for pressure determination [36]. The equation of state (EOS) of metallic Cu added to the sample was used as a second pressure gauge [37]. A 4:1 ethanol:methanol mixture was used as pressure transmitting medium. Diffraction patterns were measured (for 30–40 s each) up to 20 GPa. The indexing of the powder patterns was performed using the CHEKCELL [38], FULLPROF [39] and POWDERCELL [40] program packages.

Unpolarized room-temperature Raman scattering experiments up to 21 GPa were performed in backscattering geometry with a mDAC using a 4:1 ethanol:methanol mixture as pressure transmitting medium like in XRD experiments. Pressure was also measured by the ruby luminescence method [36]. The signal was collected by a Horiba Jobin Yvon LabRAM HR UV microspectrometer equipped with a thermoelectrically-cooled multichannel CCD detector and a

spectral resolution better than 2 cm^{-1}. A HeNe laser (632.8 nm line) with a power below 5 mW was used in order not to burn the sample.

Results

Structural characterization

The crystal structure of copper selenide eventually imparts its physical properties. In our high-pressure experiments, we have shortened the interatomic Cu – Se and Cu – Cu distances in a controlled way, inducing two different phase transitions. At ambient conditions, $Cu_{1.80(3)}Se$ adopts an aF-type structure, described by the cubic space group $Fm\bar{3}m$ and with lattice parameter *a* = 5.761(2) Å. This result is in excellent agreement with previous literature data on this specific chemical composition [5]. The intensities of the room-pressure XRD pattern accord well with an atomic arrangement where the Se atoms occupy the corners of the cubic cell (Wyckoff position 4a: (0, 0, 0)) and the Cu atoms are located at the (¼, ¼, ¼) 8c Wyckoff position with a 0.9 partial occupation factor.

The XRD patterns collected at high pressure present texturing effects due to uneven crystal sizes of the powder samples and preferred orientations of the crystals (see Figure 2, at 0.9 GPa). This effect occurs when the sample is loaded in the diamond-anvil cell, even if exhaustively ground in a mortar with a pestle, and entails that the relative intensities of the diffraction maxima are not accurate to perform full structural refinements for copper selenide in the case of our experiment. Therefore, only peak positions could be used to the structural analysis which allow us to accurately infer the lattice parameters of the compound upon compression. Figure 2 shows the raw cake image and the LeBail profile-fitting refinement of the initial cubic anti-fluorite structure of $Cu_{1.80(3)}Se$ at 0.9 GPa, to illustrate the quality of our data. Figure 3 shows the angle-dispersive synchrotron XRD data for $Cu_{1.80(3)}Se$ at several selected pressures, giving an idea of the phase stability ranges of this compound under compression. Indexations of the powder XRD patterns evidenced that this structure is stable up to 2 GPa. The lattice parameter of the low-pressure aF phase at different pressures are collected in Table I, and the evolution of the volume per formula unit is shown in Figure 4. We used a second-order Birch–Murnaghan EOS [41] to fit our pressure–volume data and we obtained a zero-pressure volume V_0 = 191.19(5) $Å^3$, and a bulk modulus B_0 = 56.5(11) GPa. The compressibility of this Cu-defective β cubic phase is smaller than that recently reported for α-Cu_2Se (B_0 = 33.5(8) GPa) and similar to the first high-pressure phase of stoichiometric copper selenide (B_0 = 52.0(7) GPa) [16]. However, the compressibility of $Cu_{1.80(3)}Se$ is larger, but compatible, to that of Cu_2S chalcocite (B_0 = 72(1) GPa) [42,43]. This is likely because Se atoms are more deformable than S atoms. The fittings of Birch–Murnaghan EOSs to the volume-pressure data of the low-pressure phases of silver selenide, Ag_2Se, and telluride, Ag_2Te, yielded B_0 = 73.5(11) GPa (and B'_0 = 3.8(4), 3rd-order) [44] and 66.48(7) GPa [45], respectively, which are higher values than those of copper selenide. Note also that these bulk moduli cannot be compared to those of the low-pressure phases of other M_2S transition metal chalcogenides either because their first pressure-induced phase transitions occur at very low pressures (CuAgS, Ag_2S) [31,32] or because their compressibility rapidly decreases with increasing pressure, having large values of the first-pressure derivative of the bulk modulus, B'_0 (Au_2S has a bulk modulus of 18.6(11) GPa, but a B'_0 value of 6.3(5)) [46].

At 2.3 GPa, the XRD pattern does not correspond to the aF phase anymore. The large amount of diffraction peaks observed at this pressure could be due to the existence of a complex intermediate structure or the coexistence of several phases. Above 4.7 GPa, a new high-pressure HP1 phase stabilizes (see Figure 3). The diffraction peaks (20 lines) at this pressure could be indexed with an orthorhombic cell with lattice constants: *a* = 17.974(9) Å, *b* = 14.829(10) Å, and *c* = 7.624(5) Å (V = 2032.07 A^3), which would entail a unit-cell content of 48 formula units. Such unit-cell would imply a volume change of about 6% at the transition. Due to the limited quality of x-ray diffraction patterns after the phase transition, we were unable to unambiguously extract the systematic extinctions and unequivocally determine the space group. A tentative structure has been obtained by the Endeavour software [47], which provides a structure solution using a combined global optimization of the difference between calculated and observed diffraction data and of the potential energy of the system. This software has been successfully used in the past to determine raw crystal structure solution of high-pressure phases [48]. We input the intensities of the XRD pattern (once masked the strong diffraction spots), the aforementioned unit-cell parameters and the possible space groups, and the best solution was described by a $P2_12_12_1$ space group. The atomic coordinates of the tentative HP1 structure are collected in Table S1 of supplementary material. This atomic arrangement should be the starting configuration for a Rietveld refinement, but the strong texturing effects prevent the full structure determination. Note, however, that the calculated intensities for this tentative structure are not far from those experimentally observed (see Fig.1S of supplementary material). The equation of state of this first high-pressure phase is defined by the following characteristic parameters: V_0 = 2105(5) $Å^3$, B_0 = 124(6) GPa and B'_0 fixed to 4 (see Fig. 4). Indexed lattice parameters of this phase at different pressures are collected in Table II. Figure 5 shows the raw cake diffraction image to illustrate the quality of our data, together with the LeBail fit using the HP1 phase.

HP1 phase is stable up to ~8.7 GPa. At 9.1 GPa (see Fig. 3), new diffraction peaks appeared and the peaks of the first high-pressure phase disappeared completely. The stability of the pattern profile during several pressure points after this pressure clearly indicates the completion of a new structural pressure-induced transition to HP2 phase. The indexation of the position of 18 diffraction peaks yielded a monoclinic solution with lattice parameters *a* = 5.375(9) Å, *b* = 11.621(6) Å, *c* = 4.968(10) Å and β = 94.7(3)º. The unit cell volume, 309.3(13) $Å^3$, is compatible with the existence of 8 $Cu_{1.80}Se$ formula units (Z = 8) per cell. As can be seen in Figure 6, the number of diffraction lines decreases compared to HP1 phase. This second pressure-induced transformation is also a first-order transition with a volume collapse of about 5.9(1) % (see Fig. 4). We proceed in the same way as described above to try to find a plausible atomic arrangement for the HP2 phase. That is, we entered the unit-cell parameters, a possible space group, the chemical composition and the powder diffraction data into the Endeavour software and let it perform the structure solution calculation. A tentative structure is proposed (see the atomic coordinates in Table 2S of the Supplementary Material and the comparison between the experimental and calculated intensities in Figure 2S). Note that these are just attempts to find the high-pressure crystal structures with powder diffraction data of limited quality, and that single-crystal XRD data will be required to unequivocally determine the structure of these two high pressure $Cu_{1.80(3)}Se$ phases. A second-order Birch-Murnaghan EOS was fitted to our HP2 pressure-volume data, obtaining a zero-pressure volume V_0 =330.6(4) $Å^3$ and a bulk modulus B_0= 120(2) GPa. Note that the HP2 phase

has a similar bulk modulus, within the uncertainties, to that of the HP1 phase. The bulk moduli of HP1 and HP2 phases of $Cu_{1.80(3)}Se$ are comparable to other high-pressure phases of copper chalcogenides, like HP2-Cu_2S (B_0 =113(7) GPa) [42] or HP1-CuAgS (B_0 =104(3) GPa) [31].

The structural behavior under compression of stoichiometric Cu_2Se was recently studied by Zhang and coworkers using XRD experiments combined with Calypso ab initio total-energy calculations [25]. They reported two pressure-induced phase transitions at 3.3 and 7.4 GPa, which are close to those we found in $Cu_{1.80(3)}Se$. Zhang et al. stated that the initial low-pressure C2/c Cu_2Se phase first transforms into a mixture of two different C2/m monoclinic phases and, subsequently, into an orthorhombic $Pca2_1$ phase. We have checked if any of these phases could explain our XRD patterns without success. Therefore, we can tentatively conclude that the structural sequence under pressure of both stoichiometric and Cu-defective copper selenides is compositionally dependent.

Our experiments evidenced that the initial cubic aF structure is recovered upon decompression to ambient pressure (see Figure 3). The XRD pattern of the sample after pressure downstroke can be perfectly fitted with the initial $Fm\bar{3}m$ aF structure, as shown in Figure 7. This fact agrees with the lack of disproportionation reactions found by Murray and Heyding [11] and rules out the disproportionation reactions of allegedly cubic Cu_2Se berzelianite structure reported by Hinze and Neuhaus [9]. These authors suggested that Cu_2Se berzelianite transformed firstly into Cu and Cu_3Se_2 umangite at 2.2 GPa, this latter phase converting at 3.7 GPa into $CuSe_2$ marcasite-type and more Cu via disproportionation. These reactions would be incompatible with the recovery of the initial structure after decompression. Note that our experiment design would prevent us to discern if a small amount of Cu was present as a disproportionation product, since we used Cu as pressure gauge. Nevertheless, this seems not to be the case, since recent experiments reported by Zhang et al. on monoclinic C2/c Cu_2Se did not find any trace of disproportionation and they recovered the initial low-pressure structure after pressure release from 42.1 GPa [25].

Vibrational characterization

In order to help in the identification of the phase transitions we performed Raman scattering (RS) measurements under compression. RS spectra at selected pressures up to 21.4 GPa are presented in Figure 8. Up to 3.7 GPa it is not possible to identify any peak related to Raman modes. This is consistent with the cubic aF structure of $Cu_{1.80(3)}Se$, since no Raman-active modes are expected for atoms located at 4a and 8c Wyckoff positions [49]. At 4.2 GPa, it is possible to detect two peaks: a broad small peak at 214.1 cm^{-1} (Peak 1 in Fig. 8) and another broad peak at 108 cm^{-1} (Peak 2 in Fig. 8). The appearance of these two peaks is indicative of the first phase transition to the HP1 phase. Increasing the pressure, the intensity of these peaks increase and they become more defined. Above 8.3 GPa, Peak 1 presents a “shoulder” which evolves to a more defined peak at 10 GPa (Peak 3). In addition, it is possible to observe the growth of four new peaks (peaks 4 to 7 in Figure 8). This is an indicative of the new transition to the HP2 phase. At 13.4 GPa it is possible to detect a slightly intense peak at 82 cm^{-1} that disappears at 16.3 GPa (Peak 5). The disappearance of this peak may be related to the fact that the intensity of the tail below 50 cm^{-1} becomes intense and probably overlaps with Peak 5. On downstroke to room pressure, all peaks

disappear (see top RS in Fig. 8), thus confirming the reversibility of pressure-induced phase transitions.

It is also interesting to note that the Raman-active modes of the HP1 and HP2 structures have frequencies below 260 cm^{-1} as expected for Cu-Se compounds. In fact, modes close to 260 cm^{-1} can be attributed to Cu-Se vibrations since they have been observed in CuSe, Cu_2Se and $CuSe_2$ samples [50-54].

Figure 9 presents the dependence of the experimental frequencies of the Raman peaks of $Cu_{1.80}Se$ at HP. In order to facilitate the identification of the peaks, we used the same numerical labels as in Figure 8. To obtain the pressure coefficient of the peaks, we fit the pressure evolution of the peaks with a linear function. It can be observed that there is a clear change in the pressure coefficient of Peaks 1 and 2 at ~7 GPa. For this reason, the linear fit of these peaks was made in two pressure ranges: from 4.2 GPa to 7.0 GPa and from 8.0 to 21.4 GPa. For the other peaks, the fit was performed over the entire range where they are observed. As can be observed in Table IV, from 4.2 GPa to 7.0 GPa, Peaks 1 and 2 present a relatively high pressure coefficient (4.3 cm^{-1}/GPa and 2.5 cm^{-1}/GPa, respectively). Above this pressure, there is a significant decrease in the pressure coefficient of these peaks and they become similar to the pressure coefficient of the other new peaks (1.8 cm^{-1}/GPa and 1.5 cm^{-1}/GPa, respectively).

It must be noted that the different pressures found for the two phase transitions in XRD and RS measurements is not strange. Usually RS measurements yield smaller phase transitions pressures than XRD measurements due to the more local nature of RS measurements than of XRD measurements [55]. This explains why the HP1-HP2 phase transition is found at a lower pressure (~8 GPa) in RS measurements than in XRD measurements (~8.7 GPa). However, the observation of a pressure-induced phase transition could be delayed in RS measurements with respect to XRD measurements if either the low- or high-pressure phases shows no Raman-active modes. In such a case, a progressive increase or decrease of the intensity of Raman modes occurs that can lead to an overestimation of the onset of the phase transition pressure, as it occurs for the aF-HP1 phase transition in $Cu_{1.80(3)}Se$, where XRD measurements suggest a phase transition around 2.9 GPa while RS measurements do not detect it below 4.2 GPa.

In summary, the results of RS measurements support the two phase transitions observed by XRD measurements. In order to elucidate the nature of each vibrational mode and to better understand the pressure-induced phase transition mechanisms, future work involving a much precise determination of the high-pressure phases in combination with theoretical calculations should be performed.

Conclusions

The structures of copper chalcogenides have narrow compositional-dependent stability ranges. In the Cu – Se system, the stoichiometric Cu_2Se and Cu-defective $Cu_{1.8}Se$ crystallize in two different phases, α and β, respectively [5,6]. This study contributes to the exploration of the structural complexity of copper selenides, modifying the atomic framework of the initial cubic $Cu_{1.80(3)}Se$ antifluorite-type structure by means of quasi-hydrostatic pressures obtained in diamond-anvil cells. In situ synchrotron X-ray diffraction and Raman spectroscopy data show the existence of two

pressure-induced phase transitions at 2.9 and 8.7 GPa to an orthorhombic and a monoclinic structure, respectively. These high-pressure phases are different from those previously reported for stoichiometric Cu_2Se, indicating that a fraction of 10% Cu vacancies produces a set of novel structural transformations upon compression. The compressibilities of the three phases were also determined from experimental data, with bulk moduli B_0(LP) = 56.5(11)GPa, B_0(HP1) = 124(6)GPa, and B_0(HP2) = 120(2) GPa. This compressional behavior is similar to that of other transition metal-rich chalcogenides, in which the metal-metal distances are comparable to those of the corresponding metallic elements.

Acknowledgments

This work has been performed under financial support from Spanish MICINN under projects MAT2016-75586-C4-2/3-P, FIS2017-83295-P, and PGC2018-097520-A-I00, as well as under the MALTA Consolider Team network (RED2018-102612-T), from Generalitat Valenciana under project PROMETEO/2018/123-EFIMAT, and from Brazilian Conselho Nacional de Desenvolvimento Científico e Tecnológico (CNPq) under projects 307199/2018-5, 422250/2016-3, and 201050/2012-9. D.S-P. and J.A.S. acknowledge the financial support of the Spanish MINECO for the RyC-2014-15643 and RyC-2015-17482 Ramon y Cajal Grants, respectively. We also thank ALBA synchrotron for funded experiments.

Literature

[1] T. Ishikawa, S. Miyatani. J. Phys. Soc. Japan 42 (1977) 159.
[2] H. Liu, X. Shi, F. Xu, L. Zhang, W. Zhang, L. Chen, Q. Li, C. Uher, T. Day, G.J. Snyder. Nature Materials 11 (2012) 422-425.
[3] D. Byeon, R. Sobota, K. Delime-Codrin, S. Choi, K. Hirata, M. Adachi, M. Kiyama, T. Matsuura, Y. Yamamoto, M. Matsunami, T. Takeuchi. Nature Commun. 10 (2019) 72.
[4] R.A. Hussain, I. Hussain. Solid State Sci. 100 (2020) 106101.
[5] A. Tonejc. J. Mater. Sci. 15 (1980) 3090–3094.
[6] A.N. Skomorokhov, D,M. Trots, M. Knapp, N.N. Bickulova, H. Fuess. J. Alloys. Compds. 421 (2006) 64-71.
[7] W. Bochert. Z. Kristallogr.106 (1945) 5-24.
[8] J.W. Earley. Amer. Mineral. 35 (1950) 337-364.
[9] E. Hinze, A. Neuhaus. Naturwissenschaften 56 (1969) 136-136.
[10] A.L.N. Stevels, F.Jellinek. Rec. Trav. Chim. Pays-Bas 90 (1971) 273.
[11] R.M. Murray, R.D. Heyding. Can. J. Chem. 53 (1975) 878.
[12] Z. Vucik, O. Milat, V. Horvatic, Z. Ogorelec. Phys. Rev. B 24 (1981) 5398.
[13] S. Kashida, J. Akai J. Phys. C: Solid State Phys. 21 (1988) 5329-5336.
[14] L. Gulay, M. Daszkiewicz, O. Strok, A. Pietraszko. Chem. Met. Alloys 4 (2011) 200-205.
[15] E. Eikeland, A.B. Blichfeld, K.A. Borup, K. Zhao, J. Overgaard, X. Shi, L. Chen, B.B. Iversen. IUCrJ 4 (2017) 476-485.
[16] H.T.J. Evans. Nature 232 (1971) 69-70.
[17] J. Haines, J.M.Leger, G. Bocquillon. Ann. Rev. Mater. Res. 31 (2001) 1-23.
[18] D. Santamaria-Perez, C. McGuire, A. Makhluf, A. Kavner, R. Chulia-Jordan, J. Pellicer-Porres, D. Martinez-Garcia, A. Doran, M. Kunz, P. Rodriguez-Hernandez, A. Muñoz. Inorg. Chem. 55 (2016) 10793-10799.

[19] D. Santamaria-Perez, C. McGuire, A. Makhluf, A. Kavner, R. Chulia-Jordan, J.L. Jorda, F. Rey, J. Pellicer-Porres, D. Martinez-Garcia, P. Rodriguez-Hernandez, A. Muñoz. Nature Commun. 7 (2016) 13647.
[20] M. Murakami, K. Hirose, K. Kawamura, N. Sata, Y. Ohishi. Science 304 (2004) 855-858.
[21] D. Santamaria-Perez, T. Marqueño, S. MacLeod, J. Ruiz-Fuertes, D. Daisenberger, R. Chulia-Jordan, D. Errandonea, J.L. Jorda, F. Rey, C. McGuire, A. Mahkluf, A. Kavner, C. Popescu. Chem. Mater. 29 (2017) 4502-4510.
[22] D. Santamaria-Perez, J. Ruiz-Fuertes, M. Peña-Alvarez, R. Chulia-Jordan, T. Marqueño, D. Zimmer, V. Gutierrez-Cano, S. MacLeod, E. Gregoryanz, C. Popescu, P. Rodriguez-Hernandez, A. Muñoz. Sci. Rep. 9 (2019) 7898.
[23] D. Errandonea, F.J. Manjon. Progress Mater. Sci. 53 (2008) 711-773.
[24] D. Santamaria-Perez, R. Chulia-Jordan. High. Press. Res. 32 (2012) 81-88.
[25] Y. Zhang, X. Shao, Y. Zheng, L. Yan, P. Zhu, Y. Li, H. Xu. J. Alloys. Compds. 732 (2018) 280-285.
[26] A. Grzechnik, A. Vegas, K. Syassen, I. Loa, M. Hanfland, M. Jansen. J. Solid State Chem. 154 (2000) 603–611.
[27] A. Vegas, A. Grzechnik, K. Syassen, I. Loa, M. Hanfland, M. Jansen. Acta Cryst. B 57 (2001) 151–156.
[28] A. Vegas, A. Grzechnik, M. Hanfland, C. Muhle, M. Jansen. Solid State Sci. 4 (2002) 1077–1081.
[29] D. Santamaria-Perez, A. Vegas, C. Muehle, M. Jansen. Acta Cryst. B 67 (2011) 109–115.
[30] D. Santamaria-Perez, A. Vegas, C. Muehle, M. Jansen. J. Chem. Phys. 135 (2011) 054511.
[31] D. Santamaria-Perez, A. Morales-Garcia, D. Martinez-Garcia, B. Garcia-Domene, C. Muhle, M. Jansen. Inorg. Chem. 52 (2013) 355–361.
[32] D. Santamaria-Perez, M. Marques, R. Chulia-Jordan, J.M. Menendez, O. Gomis, J. Ruiz-Fuertes, J.A. Sans, D. Errandonea, J.M. Recio. Inorg. Chem. 51 (2012) 5289–5298.
[33] Z. Zhao, S. Wang, A.R. Oganov, P. Chen, Z. Liu, W.L. Mao. Phys. Rev. B 89 (2014) 180102.
[34] Y. Zhang, Y. Li, Y. Ma, Y. Li, G. Li, X. Shao, H. Wang, T. Cui, X. Wang, P.Zhu. Sci. Reports 5 (2015) 14681.
[35] A.P. Hammersley, S.O. Svensson, M. Hanfland, A.N. Fitch, D. Hausermann. High Press. Res. 14 (1996) 235–248.
[36] H.K. Mao, J. Xu, P.M. Bell. J. Geophys. Res.-Solid Earth Planets 91 (1986) 4673– 4676.
[37] A. Dewaele, P. Loubeyre, M. Mezouar. Phys. Rev. B 70 (2004) 094112.
[38] J. Laugier, B. Bochu, LMGP-Suite Suite of Programs for the interpretation of Xray Experiments, ENSP/Laboratoire des Matériaux et du Génie Physique, France, <http://www.inpg.fr/LMGP> and <http://www.ccp14.ac.uk/tutorial/ lmgp/>.
[39] J. Rodriguez-Carvajal. Physica B 192 (1993) 55–69.
[40] G. Nolze, W. Kraus. Powder Diffr. 13 (1998) 256–259.
[41] F. Birch. J. Geophys. Res. 83 (1978) 1257-1268.
[42] D. Santamaria-Perez, G. Garbarino, R. Chulia-Jordan, M.A. Dobrowolski, C. Mühle, M. Jansen. J. Alloys. Compds. 610 (2014) 645-650.
[43] D. Zimmer, J. Ruiz-Fuertes, W. Morgenroth, A. Friedrich, L. Bayarjargal, E. Haussühl, D. Santamaria-Perez, S. Frischkorn, V. Milman, B. Winkler. Phys. Rev. B 97 (2018) 134111.
[44] Z. Zhao, S. Wang, A.R. Oganov, P. Chen, Z. Liu, W.L. Mao. Phys. Rev. B, 89 (2014) 180102.
[45] Y. Zhang, Y. Li, Y. Ma, Y. Li, G. Li, X. Shao, H. Wang, T. Cui, X. Wang, P. Zhu. Sci. Rep. 5 (2015) 14681.
[46] D. Santamaria-Perez, D. Daisenberger, J. Ruiz-Fuertes, T. Marqueño, R. Chulia-Jordan, C. Muehle, M. Jansen, P. Rodriguez-Hernandez, A.Muñoz, E.R. Johnson, A. Otero-de-la-Roza. Chem. Sci. 10 (2019) 6467.
[47] H. Putz, J.C. Schoen, M. Jansen. J. Appl. Cryst. 32, (1999) 864-870.

[48] D. Santamaria-Perez, J. Haines, U. Amador, E. Moran, A. Vegas. Acta Cryst. B 62 (2006) 1019 -1024.
[49] E. Kroumova, M.I. Aroyo, J.M. Perez Mato, A. Kirov, C. Capillas, S. Ivantchev, H. Wondratschek. Phase Transitions, 76 (2003) 155-170.
[50] E. Anastassakis. Solid State Commun. 13 (1973) 1297.
[51] M. Ishii, K. Shibata, H. Nozaki. J. Sold State. Chem. 105 (1993) 504.
[52] B. Minceva-Sukarova, M. Najdoski, I. Grozdanov, C.J. Chunnilall. J. Mol. Struct. 410-411 (1997) 267.
[53] W.Witte, R. Kniese, M. Powalla. Thin Solid Films 517 (2008) 867.
[54] T. Tanaka, T. Sueishi, K. Saito, Q. Guo, M. Nishio, K.M. Yu, W. Walukiewicz. J. Appl. Phys. 111 (2012) 053522.
[55] J.M. Besson, J.P. Itié, A. Polian, G. Weill, J.L. Mansot, J. Gonzalez. Phys. Rev. B 44 (1991) 4214.

Table I – List of pressures (P), lattice parameters (a), unit-cell volumes (V) and volumes per formula unit (V/Z) from results obtained in LeBail refinements of the low-pressure cubic aF-type structure.

Pressure (GPa)	*a* axis (Å)	Unit cell Volume (Å^3)	V/Z (Å^3)
1E-4	5.761(2)	191.2(2)	47.80(5)
0.2	5.753(3)	190.4(3)	47.61(7)
0.54	5.743(3)	189.4(3)	47.36(7)
0.87	5.733(4)	188.4(4)	47.10(10)
1.5	5.712(6)	186.4(6)	46.60(15)
1E-4	5.757(2)	190.8(2)	47.70(5)

Table II – List of pressures (P), lattice parameters (a, b, c), unit-cell volumes (V) and volumes per formula unit (V/Z) from results obtained in LeBail refinements of the orthorhombic HP1 structure.

Pressure (GPa)	*a* axis (Å)	*b* axis (Å)	*c* axis (Å)	Unit-cell Volume ($Å^3$)	V/Z ($Å^3$)
4.7	17.974(9)	14.829(10)	7.624(5)	2032(3)	42.33(7)
6.1	17.919(15)	14.778(10)	7.600(4)	2012(4)	41.93(9)
7.4	17.880(14)	14.738(12)	7.580(6)	1997(5)	41.61(10)
8.3	17.851(17)	14.693(11)	7.561(6)	1983(5)	41.32(11)

Table III – List of pressures (P), lattice parameters (a, b, c, β), unit-cell volumes (V) and volumes per formula unit (V/Z) from results obtained in LeBail refinements of the monoclinic HP2 structure.

Pressure (GPa)	a axis (Å)	b axis (Å)	c axis (Å)	β angle (º)	Unit-cell Volume ($Å^3$)	V/Z ($Å^3$)
9.1	5.375(9)	11.621(6)	4.968(10)	94.70(9)	309.3(13)	38.66(16)
10	5.365(5)	11.601(5)	4.960(6)	94.67(6)	307.6(8)	38.46(10)
11.2	5.346(5)	11.580(8)	4.947(9)	94.70(7)	305.2(11)	38.15(14)
11.8	5.336(13)	11.575(9)	4.941(14)	94.65(10)	304(2)	38.0(2)
12.4	5.336(12)	11.568(9)	4.929(13)	94.68(9)	303(2)	37.9(2)
7.6	5.395(5)	11.651(7)	4.988(8)	94.72(7)	312.5(10)	39.06(12)

Table IV - Experimental pressure coefficients of Cu_2Se Raman vibrational modes obtained by a fit with the linear equation $\omega(P) = \omega_0 + a.P$ in the pressure range from 4.2 to 7.0 GPa and from 8.0 to 21.4 GPa.

Peak	4.2 – 7.0 GPa	8.0 – 21.4 GPa
	a (cm^{-1}/GPa)	*a* (cm^{-1}/GPa)
1	4.3	1.8
2	2.5	1.5
3	-	1.7
4	-	1.6
5	-	0.8
6	-	1.2
7	-	1.3

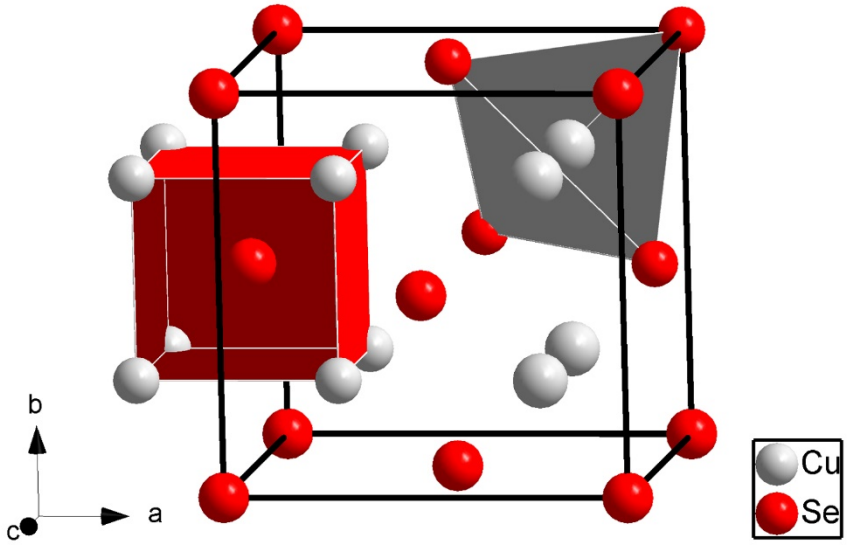

Figure 1 – Projection of Cu-defective anti-fluorite-type (aF) structure of $Cu_{1.80}Se$ at ambient conditions. The Cu positions have an occupation factor of 0.9. Thick black lines correspond to unit-cell edges. Se – Se and Cu – Cu contacts have been drawn with thin white lines to show Cu (tetrahedron in gray) and Se (cube in red) atoms coordination polyhedra.

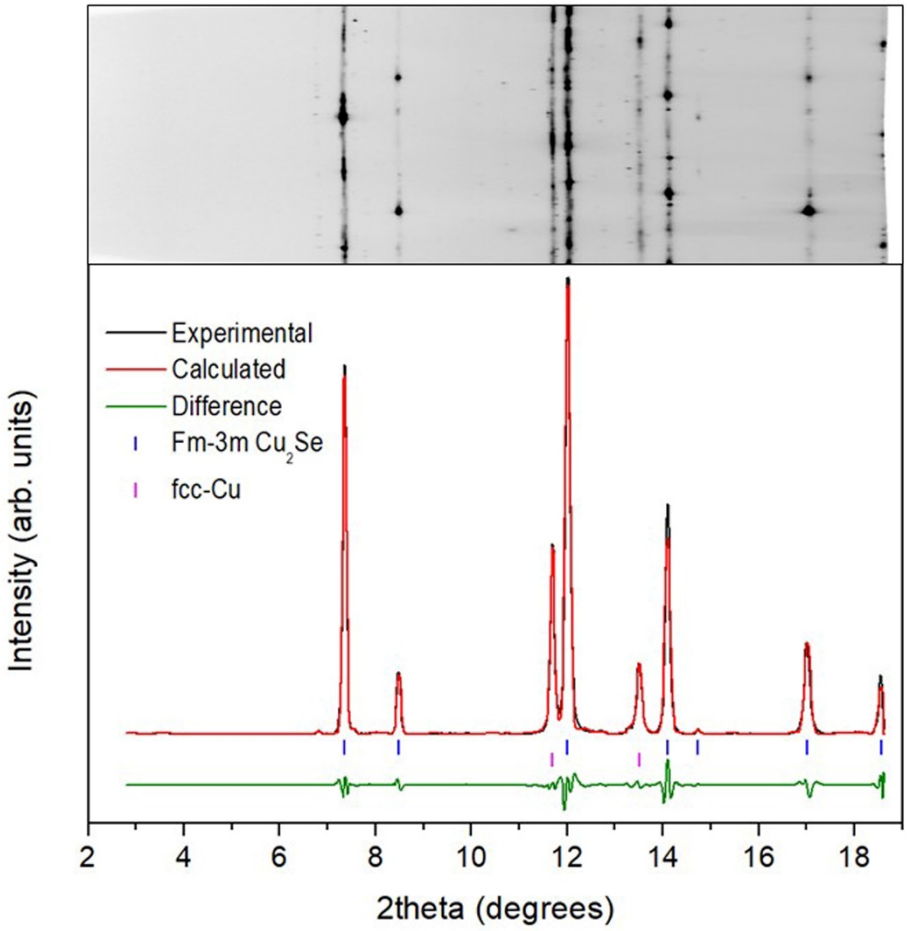

Figure 2 – (Top) Raw cake image of the diffraction signal collected in the detector at 0.9 GPa. (Bottom) LeBail fit of the integrated diffraction pattern of the ambient-temperature low-pressure aF $Cu_{1.80(3)}Se$ phase. Observed, calculated and difference X-ray diffraction profiles are depicted in black, red and green, respectively. Blue and magenta vertical marks indicate Bragg reflections of the aF $Cu_{1.80(3)}Se$ sample and the Cu used as pressure gauge.

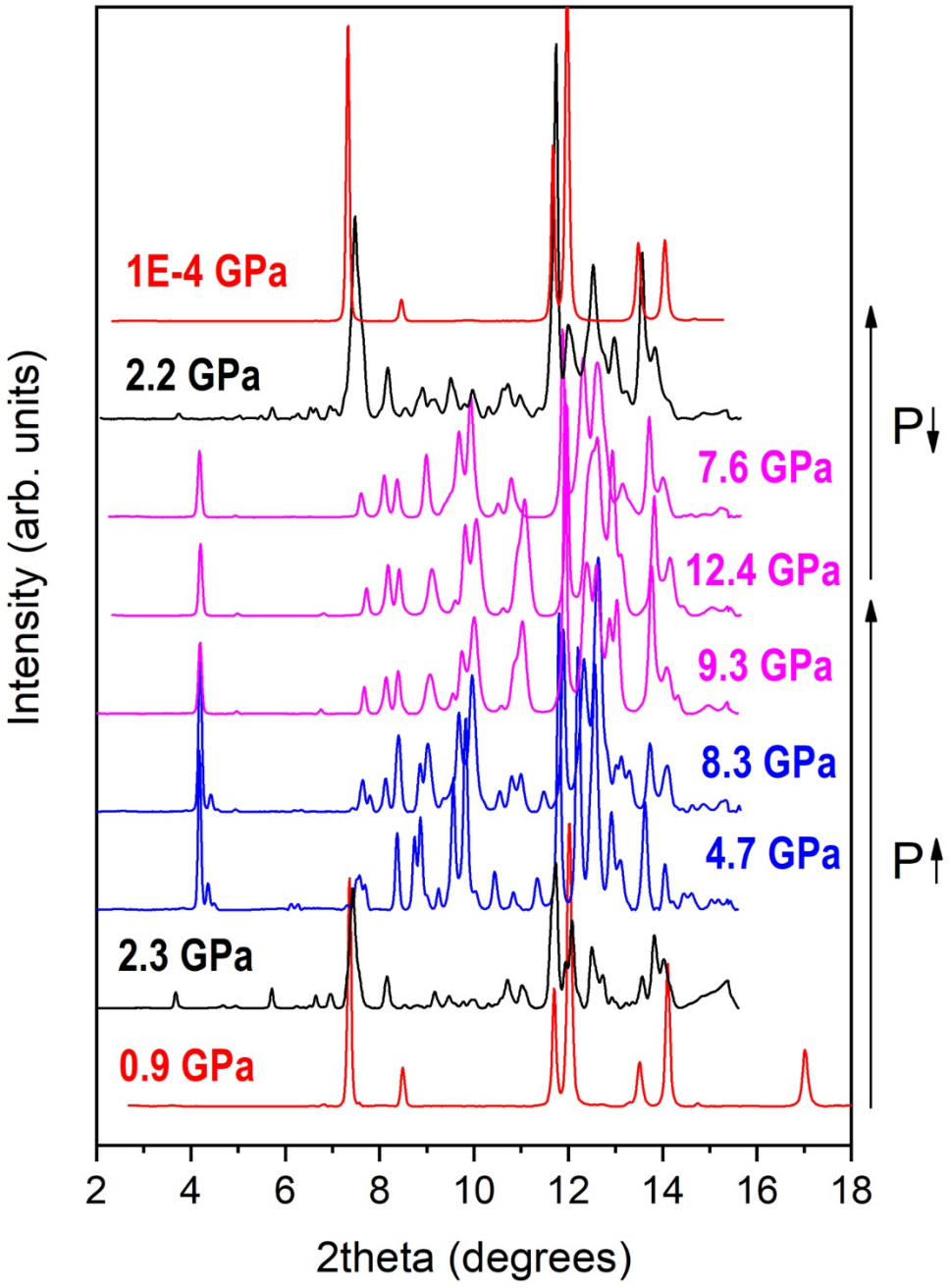

Figure 3 – X-ray powder diffraction patterns of $Cu_{1.80(3)}Se$ at different pressures. Backgrounds subtracted. Red, blue and magenta patterns represent the low-pressure aF, HP1 and HP2 phases, respectively. Sharp peaks at 2θ ~11.7-12.0º and 13.5-13.9º correspond to the (111) and (200) Cu reflections.

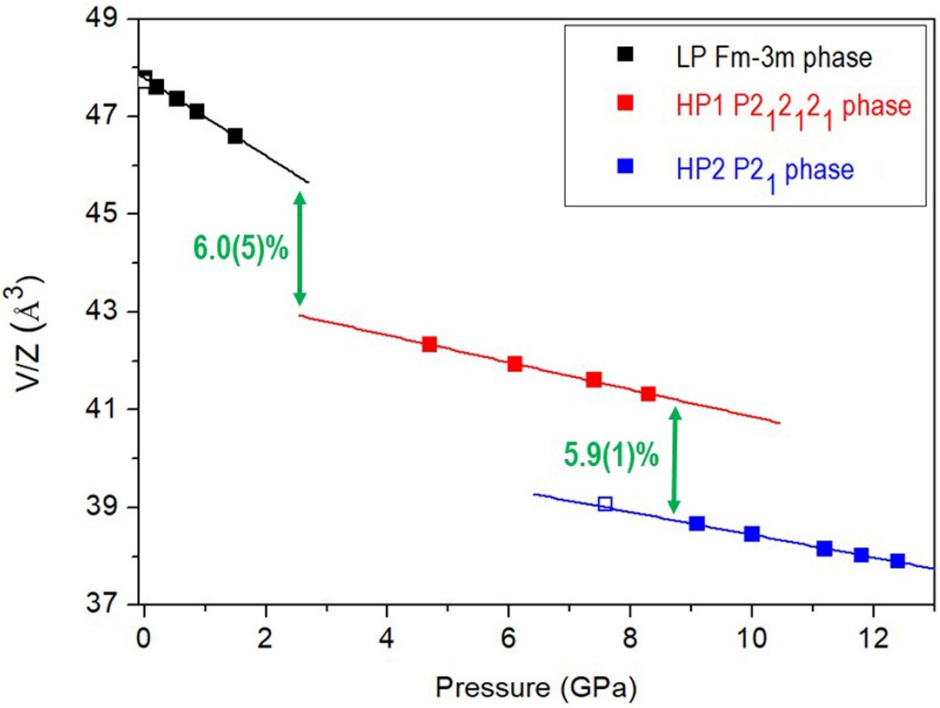

Figure 4 – Pressure dependence of the volumes per formula unit of the different phases of $Cu_{1.80(3)}Se$. Solid black, red and blue squares represent P – V data points corresponding to the low-pressure cubic aF-type, orthorhombic HP1, and monoclinic HP2 phases, respectively. The EOSs fitted are illustrated as solid lines. Empty squares correspond to pressure downstroke data points.

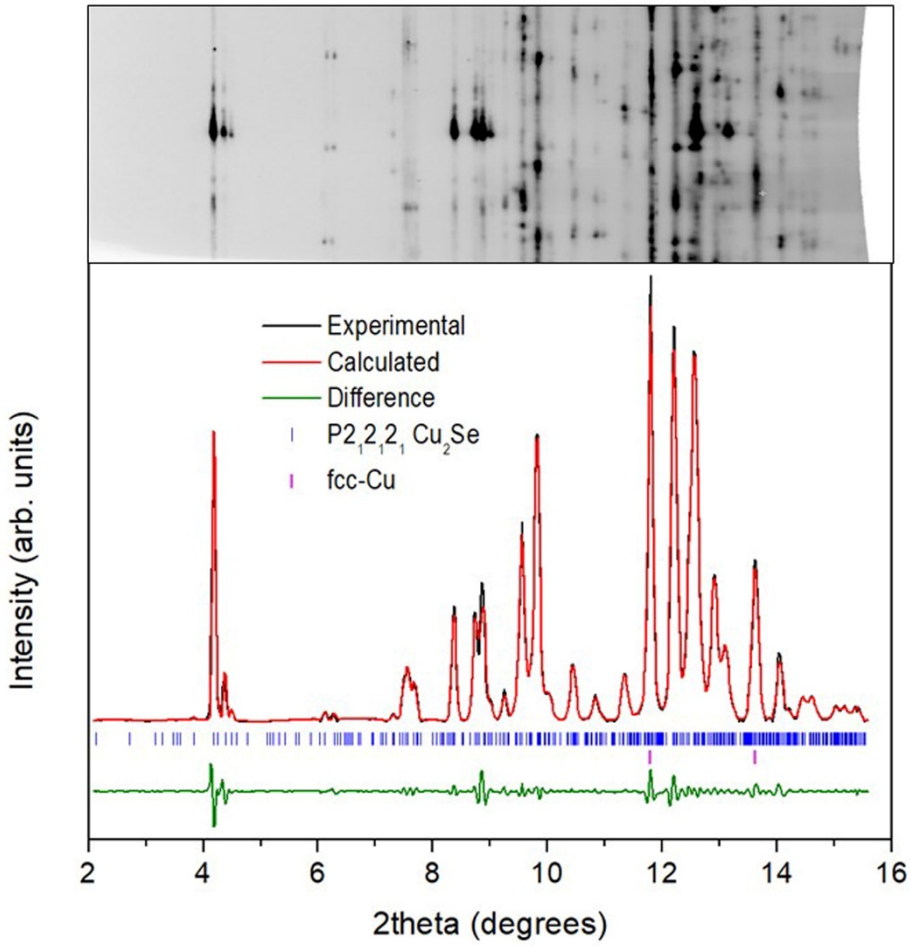

Figure 5 - (Top) Raw cake image of the diffraction signal collected in the detector at 4.7 GPa. (Bottom) LeBail fit of the integrated diffraction pattern of the ambient-temperature HP1 $Cu_{1.80(3)}Se$ phase (we used the space group $P2_12_12_1$ for the refinement). Observed, calculated and difference X-ray diffraction profiles are depicted in black, red and green, respectively. Blue and magenta vertical marks indicate Bragg reflections of the aF $Cu_{1.80(3)}Se$ sample and the Cu used as pressure gauge.

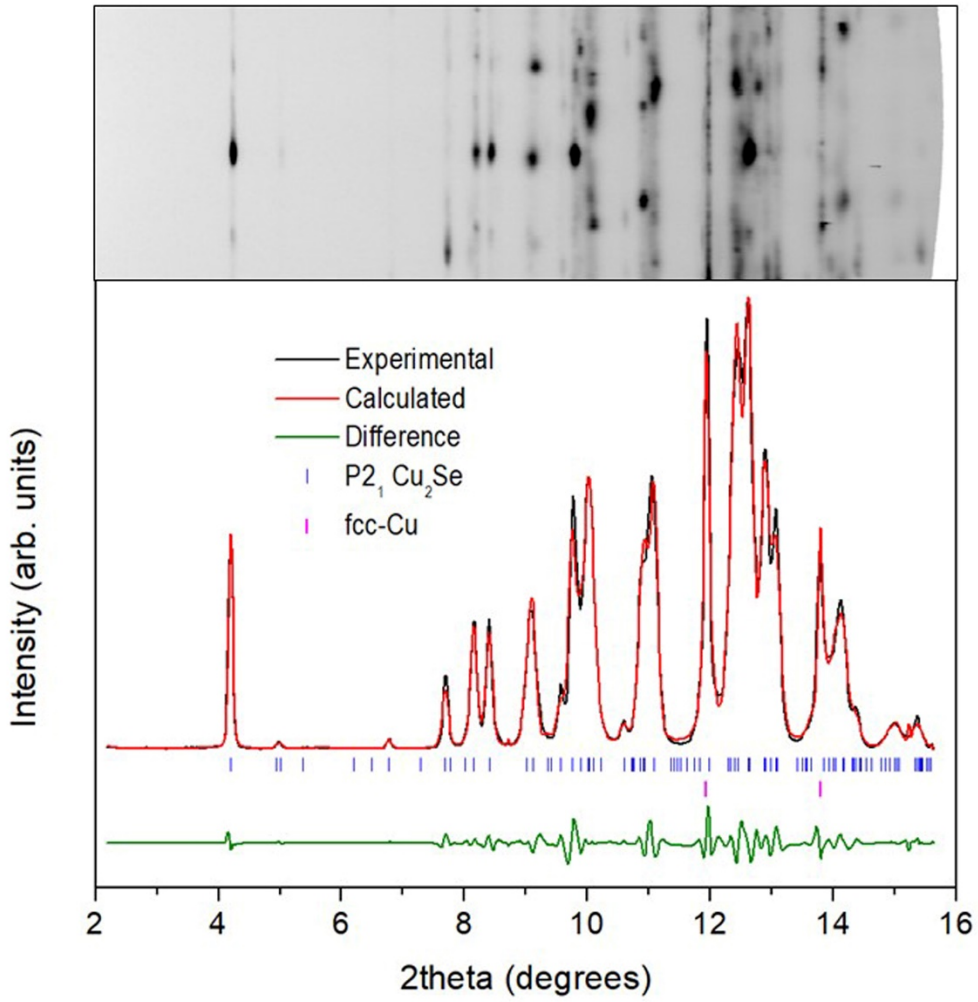

Figure 6 - (Top) Raw cake image of the diffraction signal collected in the detector at 11.2 GPa. (Bottom) LeBail fit of the integrated diffraction pattern of the ambient-temperature HP2 $Cu_{1.80(3)}Se$ phase (we used the space group $P2_1$ for the refinement). Observed, calculated and difference X-ray diffraction profiles are depicted in black, red and green, respectively. Blue and magenta vertical marks indicate Bragg reflections of the aF $Cu_{1.80}Se$ sample and the Cu used as pressure gauge.

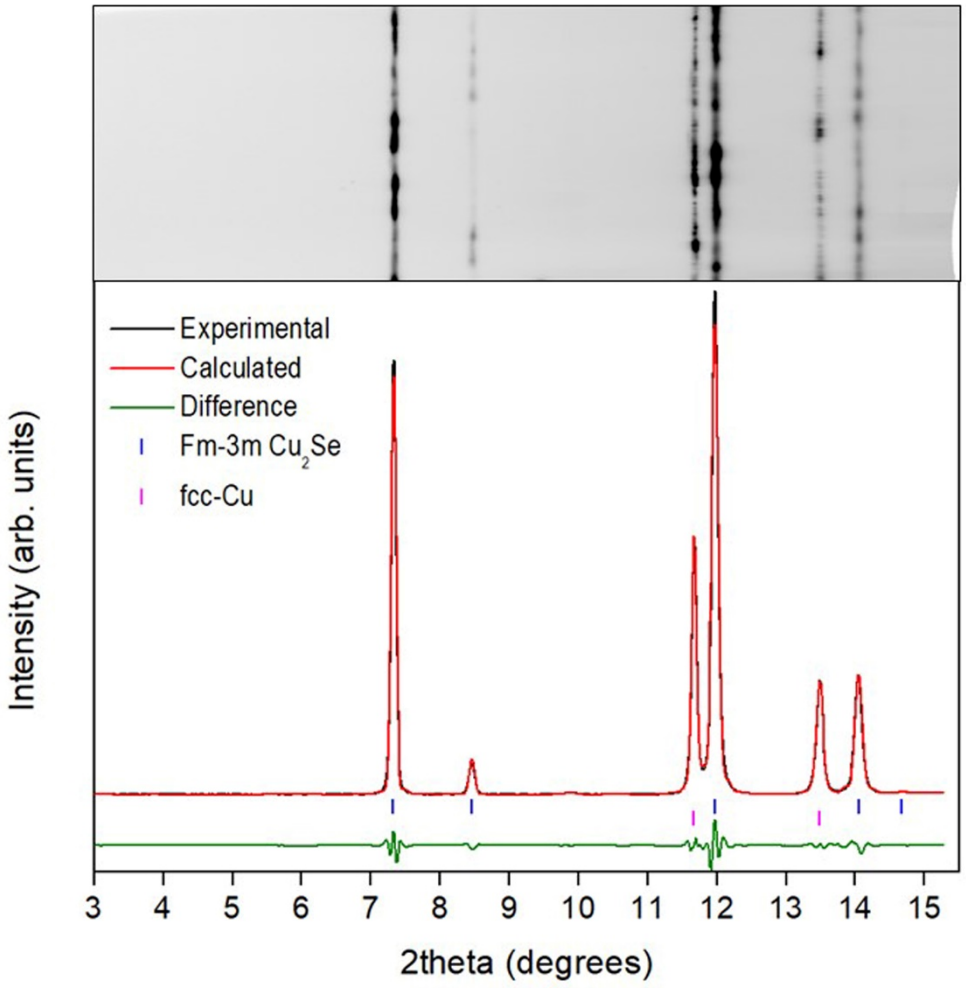

Figure 7 - (Top) Raw cake image of the diffraction signal collected in the detector at ambient conditions after decompression. (Bottom) LeBail fit of the integrated diffraction pattern of the ambient-temperature low-pressure aF $Cu_{1.80(3)}Se$ phase. Observed, calculated and difference X-ray diffraction profiles are depicted in black, red and green, respectively. Blue and magenta vertical marks indicate Bragg reflections of the aF $Cu_{1.80}Se$ sample and the Cu used as pressure gauge

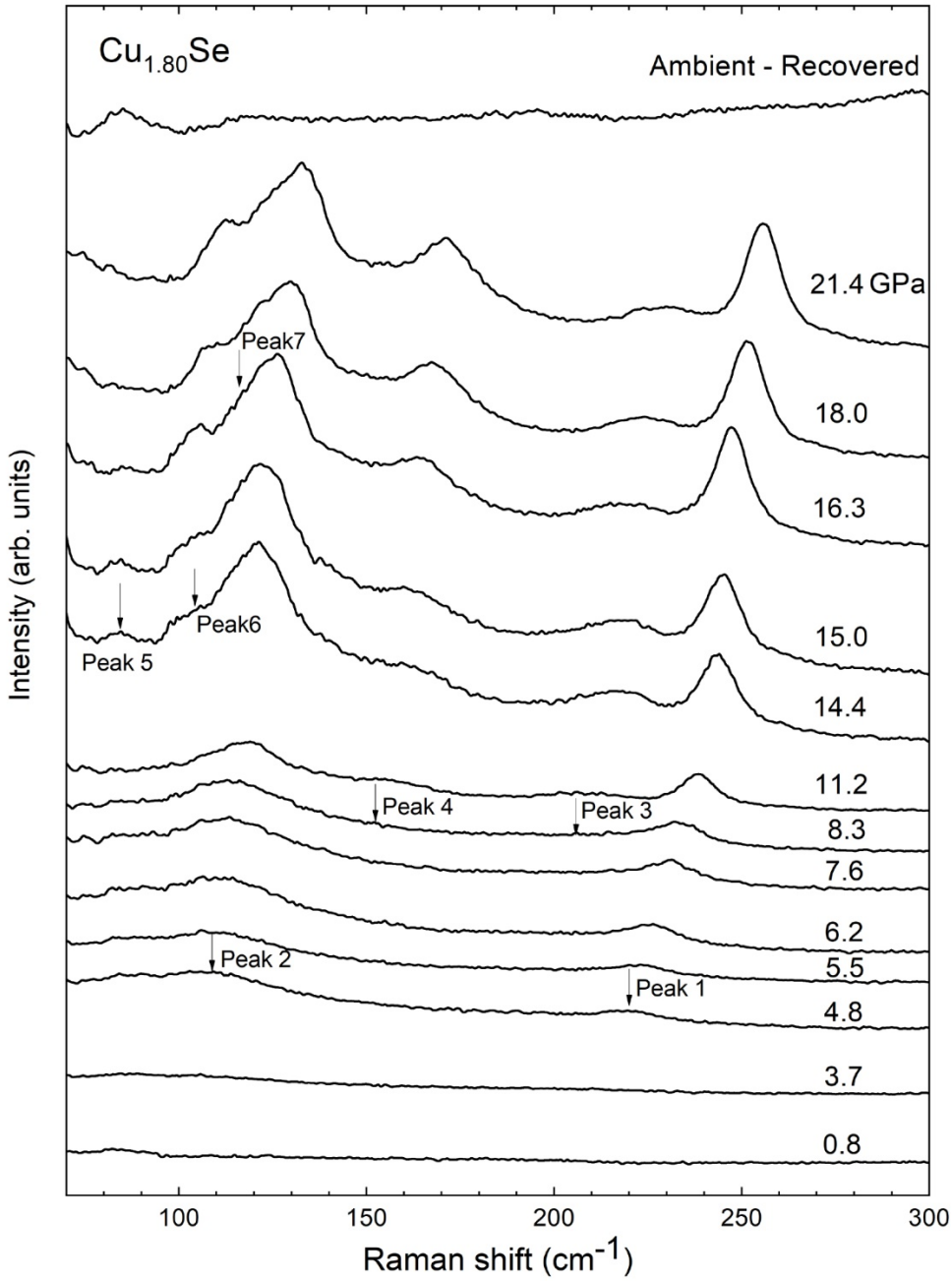

Figure 8 - Room-temperature Raman spectra of $Cu_{1.80(3)}Se$ at selected pressures up to 21.4 GPa. The top spectrum corresponds to the recovered sample after decompression. The arrows and their numbers indicate, respectively, the position and the sequence in which the new peaks are observed.

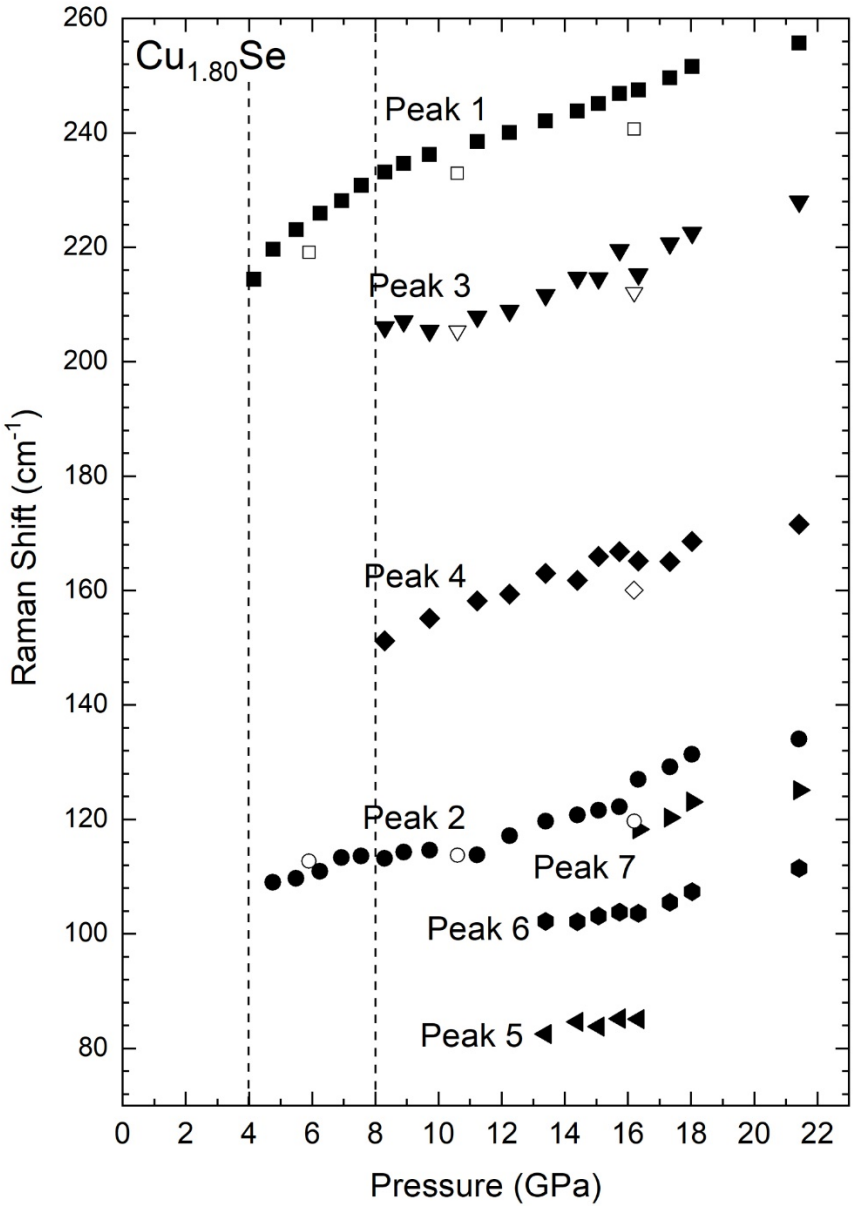

Figure 9 - Experimental pressure dependence of the Raman-active modes of $Cu_{1.80(3)}Se$. Solid (open) symbols represent the data obtained during upstroke (downstroke). The numerical identification of the peaks corresponds to that shown in Fig. 8. The vertical dashed lines at 4.0 GPa and 8.0 GPa indicate the phase transition pressures at which the first appearance of peaks 1 and 2, and the change in the pressure coefficients of peaks 1 and 2 were observed, respectively.

SUPPLEMENTARY INFORMATION

Table S1.- Atomic coordinates of the tentative $P2_12_12_1$ orthorhombic HP1 structure obtained from the Endeavour software. Lattice parameters at 4.7 GPa are a =17.974(9) Å, b =14.829(10) Å, c = 7.624(5) Å. The occupation factor of Cu positions should be 0.9 to be consistent with the $Cu_{1.80(3)}Se$ stoichiometry.

Atom	Wyck.	x	y	z
Cu	4*a*	0.01410	0.26900	0.22850
Cu2	4*a*	0.51940	0.20840	0.15260
Cu3	4*a*	0.73170	0.08280	0.20690
Cu4	4*a*	0.29150	0.70620	0.05640
Cu5	4*a*	0.18710	0.32590	0.25320
Cu6	4*a*	0.09110	0.49920	0.27450
Cu7	4*a*	0.18860	0.53080	0.06240
Cu8	4*a*	0.48200	0.35200	0.13700
Cu9	4*a*	0.58160	0.02590	0.06370
Cu10	4*a*	0.10910	0.78560	0.06860
Cu11	4*a*	0.14390	0.08940	0.19500
Cu12	4*a*	0.30040	0.01050	0.93580
Cu13	4*a*	0.04970	0.07830	0.51280
Cu14	4*a*	0.11170	0.21280	0.75590
Cu15	4*a*	0.06160	0.65010	0.34520
Cu16	4*a*	0.30940	0.27480	0.07410
Cu17	4*a*	0.38560	0.08320	0.08510
Cu18	4*a*	0.04000	0.94590	0.15690
Cu19	4*a*	0.59720	0.02820	0.39780
Cu20	4*a*	0.37780	0.36010	0.26530
Cu21	4*a*	0.25160	0.13210	0.73530
Cu22	4*a*	0.13400	0.06140	0.86090
Cu23	4*a*	0.05870	0.21470	0.46350
Cu24	4*a*	0.25580	0.14970	0.27570
Se	4*a*	0.27140	0.41970	0.23390
Se2	4*a*	0.49790	0.00380	0.27460
Se3	4*a*	0.38340	0.20460	0.26550
Se4	4*a*	0.10940	0.21650	0.11900
Se5	4*a*	0.29020	0.01600	0.58880
Se6	4*a*	0.72240	0.23770	0.12370
Se7	4*a*	0.06750	0.35580	0.47500
Se8	4*a*	0.10530	0.78260	0.39360
Se9	4*a*	0.16610	0.13650	0.51320
Se10	4*a*	0.83050	0.06120	0.09070
Se11	4*a*	0.06560	0.63580	0.02320
Se12	4*a*	0.02000	0.94050	0.42150

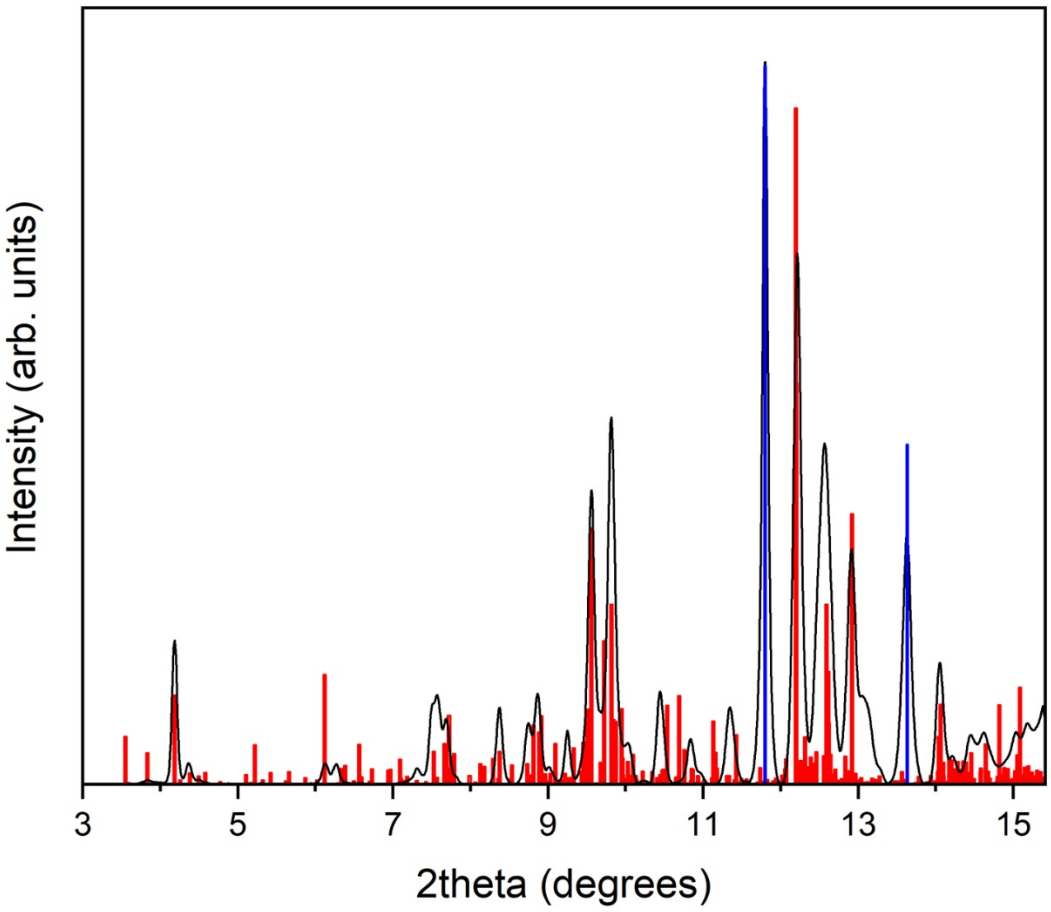

Figure 1S.- Experimental XRD pattern at 4.7 GPa (once the strongest diffraction spots are masked) compared to the calculated intensities from the tentative HP1 structure obtained by Endeavour (see Table 1S). Red and blue columns correspond to the $Cu_{1.8}Se$ phase and elemental Cu used as pressure gauge, respectively.

Table S2.- Atomic coordinates of the tentative $P2_1$ monoclinic HP2 structure obtained from the Endeavour software. Lattice parameters at 11.2 GPa are a = 5.346(5) Å, b =11.580(8) Å, c = 4.947(9) Å, β = 94.70(7)º.

Atom	**Wyck.**	**x**	**y**	**z**
Cu	2*a*	0.16475	0.84567	0.40102
Cu	2*a*	0.02132	0.35427	0.13539
Cu	2*a*	0.27936	0.50271	0.15599
Cu	2*a*	0.39272	0.02529	0.31155
Cu	2*a*	0.00548	0.07458	0.58130
Cu	2*a*	0.22667	0.20310	0.80522
Cu	2*a*	0.72263	0.20736	0.09687
Cu	2*a*	0.38932	0.34494	0.49047
Se	2*a*	0.72929	0.47548	0.13851
Se	2*a*	0.37137	0.68814	0.30749
Se	2*a*	0.17592	0.48529	0.73065
Se	2*a*	0.20875	0.19572	0.22613

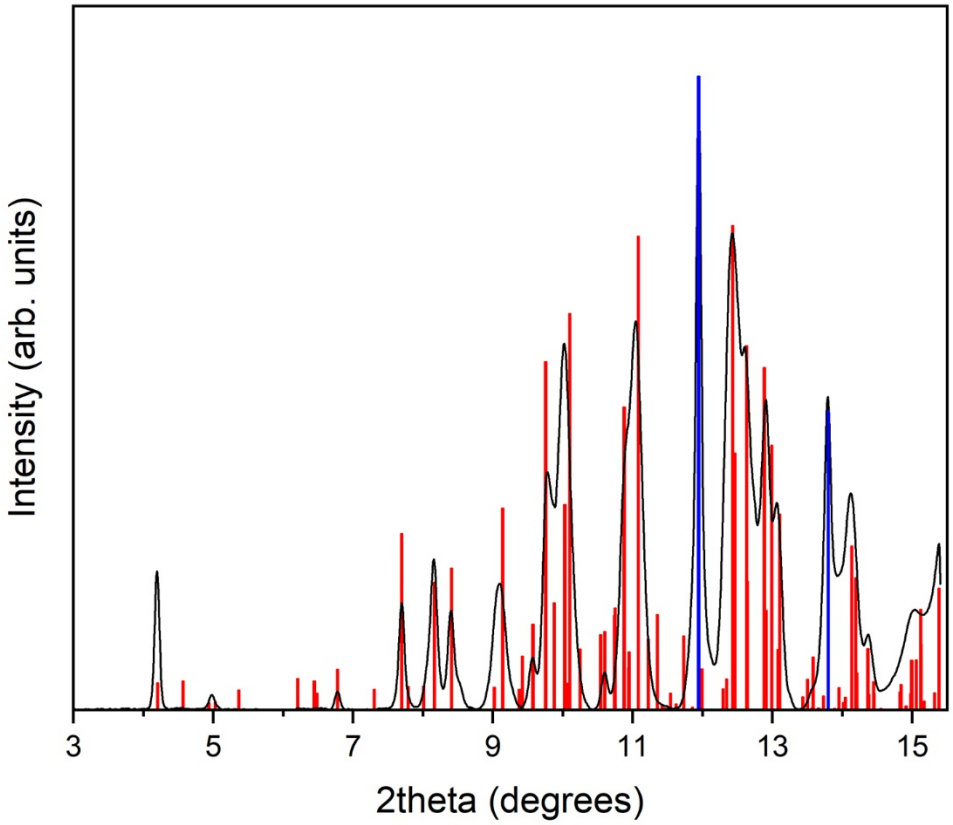

Figure 2S.- Experimental XRD pattern at 11.2 GPa (once the strongest diffraction spots are masked) compared to the calculated intensities from the tentative HP2 structure obtained by Endeavour (see Table 2S). Red and blue columns correspond to the $Cu_{1.8}Se$ phase and elemental Cu used as pressure gauge, respectively.